Check for updates

Metal-free sulfur-doped reduced graphene oxide electrocatalysts for promising production of hydrogen peroxide: construction and identification of active sites†

Sifan Li,‡[ad] Shiwen Du,‡[bc] Jiansheng Li, [ID] *[ab] Wenjun Fan,[b] Yang Yang, [ID] [b] Peng Zhao,[a] Haotian Zhu,[a] Wansheng You, [ID] [a] Xiaojing Sang [ID] *[a] and Fuxiang Zhang [ID] *[b]

Identifying and tailoring active sulfur configurations in heteroatom-doped carbon electrocatalysts for the selective $2e^-$ oxygen reduction reaction (ORR) pathway remains a significant challenge. Here we designed and synthesized sulfur-doped reduced graphene oxide electrocatalysts containing C–S and C–SO_x moieties (denoted as S_xRGO, $x = 1, 10, 20$) for promising ORR into hydrogen peroxide (H_2O_2). The optimized $S_{10}RGO$ catalyst exhibits unexpected H_2O_2 selectivity of *ca.* 90% across a wide voltage range of 0.10−0.65 V, accompanied with excellent long-term stability (40 h) in an alkaline flow cell with 90.5% H_2O_2 faradaic efficiency at an industrial current density of 300 mA cm^{-2}. Theoretical and experimental analyses integrally reveal and identify the C–S and C–SO_x groups as the main active sites in the carbon-based catalyst. Specifically, the C–S group is found to favor the formation of OOH*, while the C–SO_x group not only facilitates the desorption of OOH* but also modulates interfacial mass transport kinetics, thereby creating a favorable microenvironment for H_2O_2 generation.

1 Introduction

Hydrogen peroxide (H_2O_2), as a green oxidizer and potential liquid fuel, has been extensively used in the fields of environmental remediation, chemical synthesis and energy conversion.[1–4] Currently, the large-scale production of H_2O_2 relies on the energy and waste-intensive anthraquinone process, suffering from high cost.[5,6] In contrast, the electrocatalytic two-electron oxygen reduction reaction ($2e^-$ ORR) offers a sustainable alternative for onsite H_2O_2 production.[7] To date, precious metals such as Pt, Au, Pd and their alloys, along with non-precious metal catalysts such as Fe, Co, and Ni have been reported to exhibit remarkable selectivity towards the $2e^-$ ORR.[8–11] However, considering the scarcity of precious metals and the potential solubility of non-precious metals, significant

efforts have been dedicated to the development of metal-free heteroatom doped carbon-based materials due to their adjustable surface and electronic structure properties.[12–14]

Sulfur-doping is particularly intriguing among various metal-free dopants (B, N, O, *etc.*) owing to its unique advantages including the larger atomic radius and electron-rich characteristics.[15–18] Its incorporation not only induces spin density redistribution in the carbon skeleton but also enhances O_2 adsorption by elevating electron density, thereby reducing the overpotential for the ORR. Basically, most studies on sulfur-doped carbon materials have focused on $4e^-$ ORR activity instead of $2e^-$ ORR.[19–21] While some recent works reveal that sulfur co-doping with other heteroatoms (*e.g.*, N, F) or defects can lead to a $2e^-$ ORR process, these findings often highlight the role of sulfur atoms in modulating the electronic structure of other atoms, and the intrinsic role of sulfur moieties in the $2e^-$ ORR remains under-investigated.[22,23] The design and fabrication of efficient and stable sulfur-doped carbon materials, specifically tailored for selective $2e^-$ ORR and capable of withstanding high current densities, continues to pose a significant challenge. Moreover, in the limited reports on the $2e^-$ ORR behavior of sulfur-doped carbon materials, the construction and identification of distinct sulfur configurations, such as C–S, C–SO_x, S–H, and S–S, as well as the elucidation of the structure–activity relationship, remain underexplored. This is a demanding yet critical endeavor for the

a School of Chemistry and Chemical Engineering, Liaoning Normal University, Dalian 116029, Liaoning, China. E-mail: lijiansheng@lnnu.edu.cn; sangxj923@nenu.edu.cn

b State Key Laboratory of Catalysis, Dalian Institute of Chemical Physics, Chinese Academy of Sciences, Dalian, 116023, Liaoning, China. E-mail: fxzhang@dicp.ac.cn

c School of Physics and Materials Engineering, Dalian Minzu University, Dalian, 116023, Liaoning, China

d Department of Biochemical Engineering, Chaoyang Normal University, Chaoyang 122000, Liaoning, China

† Electronic supplementary information (ESI) available. See DOI: https://doi.org/10.1039/d5sc03069b

‡ These authors contributed equally to this work.

advancement of catalyst performance and selectivity.[24–30] Additionally, conventional studies have primarily focused on electronic structure engineering through heteroatom doping, often overlooking the potential impact on surface chemical microenvironments. Notably, recent studies have shown that adding dimethyl sulfoxide (DMSO) to electrolytes can enhance H_2O_2 selectivity by forming H_2O–DMSO hydrogen-bonding networks, which alters proton transfer kinetics and facilitates H_2O_2 production.[31] This insight provides a new perspective for understanding the electrocatalytic $2e^-$ ORR process of S-doped carbon materials.

In this work, a series of precisely engineered C–S and C–SO_x co-modified carbon-based catalysts (S_xRGO) were synthesized using graphene oxide (GO) and sulfur as precursors. The optimized $S_{10}RGO$ catalyst shows superior electrocatalytic H_2O_2 performance to most previously reported sulfur-doped carbon materials. Combined with density functional theory (DFT) calculations, a significant correlation between sulfur configurations (C–S and C–SO_x) and the $2e^-$ ORR catalytic performance was built, in which the C–S group was disclosed to favor the formation of the key oxygenated intermediate OOH*, while the C–SO_x group was shown to facilitate the desorption of OOH*. In addition, the kinetic effects of surface SO_x groups on H_2O_2 generation were studied. This work delivers the first report on the remarkable influence of distinct sulfur configurations (e.g., S–C, SO_x) on intermediate adsorption and H_2O_2 generation kinetics, which provides a clearer view and a new perspective for understanding the selectivity and activity of sulfur-doped carbon materials in the ORR, and lays a foundation for designing high-performance electrocatalysts and establishing precise control over multi-electron reaction selectivity.

2 Experimental

Synthesis of S_xRGO

Before use, GO was subjected to a series of purification steps, including washing with a 10 wt% hydrochloric acid solution, followed by rinsing with deionized water and acetone, in order to remove metal impurities. Subsequently, it was dried overnight at 40 °C in an oven. GO and sulfur sublimated powder with various mass ratios (e.g., 1 : 10 for $S_{10}RGO$) was initially ground thoroughly in an agate mortar. The prepared mixed powders were then collected into a porcelain boat and placed at the center of a tube furnace. By continuously feeding Ar gas (50 sccm), the furnace was heated up to 160 °C at a ramp rate of 2 °C min^{-1}. After keeping this temperature for 6 h, the annealing temperature was increased to 500 °C with a ramp rate of 5 °C min^{-1} and held there for 1 h, followed by natural cooling under a continuous flow of Ar gas. The collected bright black product was denoted as S_xRGO ($x = 0, 1, 10, 20$).

Synthesis of $S_{10}RGO-500$

$S_{10}RGO-500$ was prepared via the same process as $S_{10}RGO$ except that the annealing temperature was directly raised to 500 °C with a ramp rate of 5 °C min^{-1} and held there for 1 h.

Synthesis of $S_0RGO-160$ and $S_{10}RGO-160$

$S_0RGO-160$ and $S_{10}RGO-160$ were prepared via the same process as S_0RGO and $S_{10}RGO$ except that the annealing temperature was raised up to 160 °C with a ramp rate of 2 °C min^{-1} and held there for 6 h.

Rotation ring disk electrode (RRDE) test

The electrochemical experiments were performed on a CHI 760E electrochemical workstation utilizing a three-electrode system. An RRDE (Taizhou Keruite Analytical Instrument, Co., Ltd, disk area: 0.1256 cm^2) with a Pt ring (ring area: 0.1664 cm^2) was used as the working electrode, a graphite rod as the counter electrode and an Ag/AgCl electrode as the reference electrode, respectively. To prepare the catalyst ink, 3.0 mg of the obtained catalysts were mixed in 1 mL of a solution containing 980 μL of deionized water/ethanol mixed solution ($V_{water}/V_{ethanol} = 5 : 1$) and 20 μL of 5 wt% Nafion solution. The mixture was then subjected to ultrasonic treatment for 60 min to form homogeneous inks. Before measurement, the RRDE was polished with 0.30, 0.10 and 0.05 μm alumina powders (Chenhua) and then cleaned with deionized water. Subsequently, 6 μL (a loading of roughly 0.143 mg cm^{-2}) of the catalyst ink was drop-cast onto a disk electrode of the RRDE tip spinning at an initial rate of 150 rpm and advanced to 300 rpm to achieve uniform electrode coverage. Two electrolytes with pH ~13 (0.1 M KOH) and ~7 (0.1 M Na_2SO_4) were used at room temperature. All potentials measured against an Ag/AgCl electrode were converted to the reversible hydrogen electrode (RHE). The H_2O_2 productivity and selectivity were determined through linear sweep voltammetry (LSV) under O_2-saturated conditions, with a scan rate of 10 mV s^{-1} at 1600 rpm, within the potential range of 0 V to 0.90 V, while maintaining the platinum ring electrode potential at 1.30 V. The collection efficiency (N) was determined to be 0.43 by the redox reaction of $[Fe(CN)_6]^{4-}/[Fe(CN)_6]^{3-}$ according to the reported procedures.[32] The double-layer capacitance was determined from cyclic voltammograms in the non-faradaic region at different scan rates (20, 40, 60, 80 and 100 mV s^{-1}). A chronoamperometry test was performed at a disk electrode potential of 0.52 V in O_2-saturated 0.1 M KOH electrolyte with an RRDE rotating speed of 1600 rpm. The Pt ring electrode was cleaned by rapid CV scanning from 0 V to −0.3 V and the electrolyte was refreshed every 2 h during the continuous operation. The measured potentials using a three-electrode setup of RRDE have no iR compensation.

Experimental details are described in the ESI.†

H_2O_2 concentration measurement

The H_2O_2 concentrations in the electrolytes were measured by a Ce^{4+} titration method based on the following equation:

$$H_2O_2 + 2Ce(SO_4)_2 \rightarrow Ce_2(SO_4)_3 + H_2SO_4 + O_2 \qquad (1)$$

The reaction of the yellow-colored Ce^{4+} to the colorless Ce^{3+} proceeds in the presence of H_2O_2. Thus, the concentration of Ce^{4+} can be measured by UV-vis absorption spectroscopy. A

typical calibration curve was plotted by linear fitting of the absorbance values at 319 nm for Ce^{4+}.

The faradaic efficiency (FE) for H_2O_2 generation was calculated as follows:

$$FE\% = (C \times V \times F \times 2)/(i \times t) \times 100\% \qquad (2)$$

where C, V, F, i, and t are the produced H_2O_2 concentration (mol L^{-1}) in the electrolyte, the volume of electrolyte (L), Faraday constant (96 485 C mol^{-1}), the operating current (A) and the test time (s), respectively.

Electrocatalytic performance in H-type cells

The bulk electrolysis measurements were conducted with a typical H-type cell, which contains 30 mL electrolyte (0.1 M KOH) separated by a Nafion 117 membrane (Dupont), in which 10 mM EDTA was added to stabilize the produced H_2O_2. 200 μL catalyst ink was firstly coated on carbon paper (1 cm × 1 cm, Toray, TGPH090) with the loading of 600 μg cm^{-2}. The graphite rod counter electrode was separated from the working electrode and Ag/AgCl reference electrode by a Nafion 117 membrane. The electrolyte in the cathode compartment was stirred with a stirring rate of 400 rpm to guarantee that the reactant can reach the electrode surface. Chronoamperometric processes were conducted to generate H_2O_2 in the O_2-saturated electrolyte at 0.52 V. Bulk electrolysis for the H-type cell was carried out without iR compensation.

Electrocatalytic performance in a flow cell

A flow cell was constructed to replicate the actual device, and the catalyst ink was coated onto the gas diffusion electrode (GDE, 1 × 3 cm^2) by a spray gun as the cathode electrode, resulting in a loading mass of roughly 600 μg cm^{-2}. The anode electrode was constructed using titanium felt, while the anode chamber and cathode chamber were separated by a Nafion 117 membrane. The electrolyte used was 1 M KOH, to which 10 mM EDTA was added for stabilizing the produced H_2O_2.[8] The flow rate of the aqueous electrolyte was set at 8 mL min^{-1} by a peristaltic pump. High-purity O_2 was continuously supplied through the opposite side of the catalyst with a flow rate of 30 mL min^{-1}. LSV curves were performed at a scan rate of 10 mV s^{-1} and manually compensated by 100% iR effects. Electrochemical impedance spectroscopy (EIS) measurements under different biases were conducted in the flow cell in a frequency range from 0.01 Hz to 100 000 Hz with an AC amplitude of 5 mV. The electrolyte was updated before the EIS test for each system to avoid the impact of H_2O_2 accumulated in the solution during the EIS test.

Computational details

All the density functional theory (DFT) calculations were performed with the aid of the Vienna *ab initio* simulation package (VASP) based on projector augmented wave (PAW) pseudopotentials with a cut-off energy of 500 eV.[33,34] The generalized gradient approximation (GGA) with a Perdew–Burke–Ernzerhof (PBE) functional was employed to approximate the exchange

and correlation effects during the relaxations.[35,36] During structure optimizations, the convergence criterion of energy on each atom was set to 1.0×10^{-5} eV, while the force convergence threshold of each atom was set to 0.015 eV·$Å^{-1}$. The models of RGO, SO_x-RGO, S-RGO, and S/SO_x-RGO were built with a vacuum spacing of 15 Å to simulate the ORR pathway using Monkhorst–Pack grids of 3 × 3 × 1.[37] The Gibbs free energies of the ORR process were evaluated using the following equation:

$$G = E_{DFT} + E_{ZPE} - TS \qquad (3)$$

where E_{DFT}, E_{ZPE}, and TS represent the DFT-calculated electronic energy, zero-point energy, and entropy of the system, respectively.

The details of materials and characterization are provided in the ESI.†

3 Results and discussion

Synthesis and characterization

Two-step thermal annealing processes were conducted under an Ar atmosphere to obtain the target materials (S_xRGO, "x" stands for the mass ratio of sublimed sulfur *versus* GO) using GO and sublimed sulfur as precursors. As shown in Fig. 1a, during the initial ramping step at 160 °C, molten sulfur infiltrates into the GO matrix and primarily reacts with the remaining oxygen-containing functional groups in GO, which may predominantly generate sulfur oxide species. Subsequently, when the annealing temperature is increased to 500 °C, the oxygen-containing functional groups were decomposed to induce disorders and vacancies in the GO lattice, which could serve as anchoring sites for sulfur atoms forming mainly C–S groups at this step (Fig. S1 and S2†).[38] However, during the one-step thermal annealing process up to 500 °C, the final formed sulfur configurations include the S–H bond in addition to C–S and C–SO_x groups (Fig. S3†), which may result from the reaction of certain decomposed –COOH groups with sulfur under rapid ramping conditions. Here the doping state of S_xRGO can be easily adjusted by regulating the programmed heating process.

Fourier transform infrared spectroscopy (FTIR), X-ray diffraction (XRD) and Raman spectroscopy were carried out to characterize the composition and structure of the as-obtained samples. As depicted in FTIR (Fig. 1b), the peak at 1728 cm^{-1} corresponds to the C=O stretching vibration for S_xRGO ($x = 0$, 1, 10, 20). The peak shift of C=C from 1583 cm^{-1} for S_0RGO gradually to 1577 cm^{-1} for S_xRGO ($x = 1$, 10, 20, β-region) may come from the change in the surface chemistry of RGO due to sulfur doping.[39,40] The peaks assigned to C–O–C (α-region) for S_0RGO are shifted for S_xRGO ($x = 1$, 10, 20), which should be derived from the introduction of sulfur oxide species that show overlapped peaks with ether and epoxides. Besides, it is worth noting that the peak corresponding to the C–S/C=S stretching vibration appears at 670 cm^{-1} for S_xRGO ($x = 1$, 10, 20).[41] XRD patterns (Fig. 1c) show a broad diffraction peak located at $2\theta = 20–30°$ for all the S_xRGO samples, which corresponds to the (002) facets of RGO.[16] Compared to S_0RGO, the (002) diffraction peak in S_xRGO ($x = 1$, 10, 20) is prominently shifted to lower

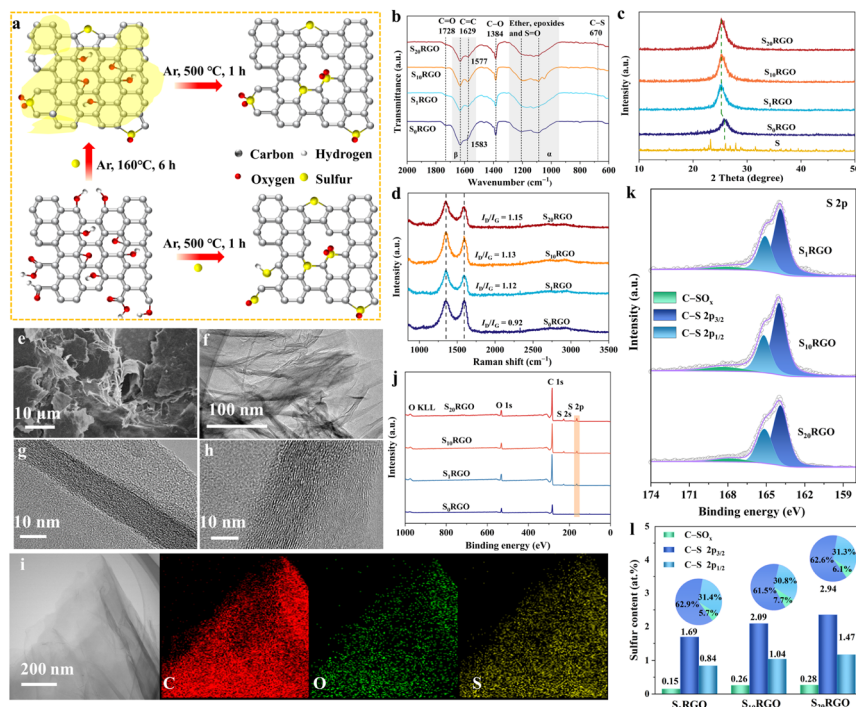**Fig. 1** (a) Schematic illustration of the preparation of catalysts. (b) FTIR spectra, (c) XRD patterns, and (d) Raman spectra of S_xRGO. (e) SEM and (f) TEM of $S_{10}RGO$. HR-TEM images of (g) S_0RGO and (h) $S_{10}RGO$, and (i) element mapping of $S_{10}RGO$. (j) Survey XPS spectra of S_xRGO. (k) S 2p XPS spectra. (l) Proportional content of each sulfur configuration (inset is the sector diagram).

angles, suggesting a lattice expansion along the (002) direction. This result further confirms the successful doping of sulfur. Additionally, the absence of any crystalline sulfur peaks in the XRD patterns of S_xRGO ($x = 1, 10, 20$) suggests that the doped sulfur is not present as crystal particles. This is consistent with the thermogravimetric results (Fig. S4†). Raman spectra (Fig. 1d and Table S1†) show that S_xRGO ($x = 1, 10, 20$) give a higher intensity ratio of D and G bands to that of S_0RGO ($I_D/I_G = 0.92$), indicating increased number of defects in the carbon materials.[42] Moreover, S_xRGO ($x = 1, 10, 20$) show a much higher electrochemically active surface area (ECSA) with respect to the S_0RGO, exposing many more active sites. Meanwhile, the S_xRGO ($x = 1, 10, 20$) samples exhibit similar ECSAs, indicating their analogous surface roughness (Fig. S5 and Table S2†). The morphology structures of S_xRGO ($x = 0, 1, 10, 20$) are similarly observed to exhibit wrinkled flakes and stacked layers according to their scanning electron microscope (SEM) and transmission electron microscope (TEM) images (Fig. 1e–i and S6–S9†). The high-resolution TEM (HR-TEM) images show that S_xRGO ($x = 1, 10, 20$) display minimal distortion in both the basal and edge regions, while the apparent layer stripes indicate that the crystalline structure of RGO is maintained after the sulfur doping process, coinciding with the XRD and Raman results. The elemental mapping of S_xRGO ($x = 1, 10, 20$) reveals a uniform distribution of sulfur within the RGO sheets, encompassing both the basal and edge regions.

The surface elements and the chemical states of S_xRGO were detected by X-ray photoelectron spectroscopy (XPS) analysis (Table S3†). Apparently, sulfur signals were observed in the XPS

survey spectra of S_xRGO ($x = 1, 10, 20$) (Fig. 1j), indicating the successful incorporation of S species into RGO. No other elements than C, O, and S were detected. The atomic sulfur content in S_xRGO ($x = 1, 10, 20$) samples increases proportionally with the increase of the S/GO mass ratio, which agrees with the results obtained from elemental analysis (Table S4†). The specific sulfur configuration in S_xRGO was further analyzed using S 2p XPS spectra (Fig. 1k), in which three deconvoluted peaks were obtained with the binding energies located at 165.2 ± 0.1, 164 ± 0.1 and 167.5–170 eV, respectively. The first two peaks are assigned to the S $2p_{1/2}$ and S $2p_{3/2}$ of the C–S group, while the latter peak corresponds to the C–SO$_x$ group.[43] This result further proves the simultaneous construction of C–S and C–SO$_x$ groups in the RGO, consistent with the FTIR results. According to their peak areas (Fig. 1l), the content of the C–S moiety is found to be gradually increased for S_1RGO (2.53 at%), $S_{10}RGO$ (3.13 at%) and $S_{20}RGO$ (4.41 at%), while the content of the C–SO$_x$ group is sharply improved from 0.15 at% for S_1RGO to 0.26 at% for $S_{10}RGO$, and then slightly rises to 0.28 at% for $S_{20}RGO$. This interesting phenomenon was deduced to result from the fact that the C–SO$_x$ group is primarily formed through the reaction of molten sulfur with the oxygen-containing functional groups at the sheet edges of GO during the initial annealing step at 160 °C, while the C–S moiety is generated from the anchoring of sulfur atoms by the vacancies in the bulk matrix of GO during the second annealing step. Besides, the contents of C–S and C–SO$_x$ configurations in the S_xRGO ($x = 1, 10, 20$) could also be revealed by analyzing the C 1s and O 1s XPS spectra (Fig. S10, S11 and Table S5†). It is worth noting that the

configuration and content of sulfur-containing groups in the carbon material could be effectively adjusted through the programmed annealing process.

Electrocatalytic ORR performances

The electrocatalytic ORR performances of S_xRGO were assessed *via* measuring the LSV curves with an RRDE as a working electrode at 1600 rpm in an O_2-saturated 0.1 M KOH (Fig. S12–S14†). As shown in Fig. 2a, the larger ring current of S_xRGO ($x = 1, 10, 20$) compared to that of S_0RGO indicates the critical role of sulfur moieties in enhancing $2e^-$ ORR activity. Fig. 2b presents the H_2O_2 selectivity and electron transfer number (n) of S_xRGO. Notably, the $S_{10}RGO$ exhibits an H_2O_2 selectivity of over 90% and an electron transfer number below 2.2 in a wide potential range from 0.10 to 0.65 V. It delivers a maximum H_2O_2 selectivity of 98.9% and a minimum n value of 2.0 at 0.52 V, surpassing most previously reported carbon-based and/or noble-metal-based electrocatalysts (Fig. 2c and Table S6†). Comparatively, the S_0RGO, S_1RGO and $S_{20}RGO$ produce the H_2O_2 selectivities of 51–73%, 81–96% and 77–95% from 0.10 to 0.65 V, accompanied with the electron transfer numbers of 3.0–2.5, 2.4–2.0 and 2.5–2.1, respectively. The electron transfer numbers for S_xRGO ($x = 0, 1, 10, 20$) obtained by the Koutecky–Levich (K–L) analysis are similar to those obtained by the RRDE method (Fig. S15 and S16†). It is noteworthy that, as shown in

Fig. 2a, unlike the S_0RGO catalyst, which exhibits a decreased ring current density at potentials below 0.3 V, the sulfur-doped catalysts, particularly $S_{10}RGO$, demonstrate a slightly increased ring current density in the same potential range. This observation suggests that sulfur-doping can facilitate the formation of H_2O_2 in the low-potential region. Besides, $S_{10}RGO$ delivers an early onset potential of 0.773 V, surpassing those of S_1RGO (0.762 V), $S_{20}RGO$ (0.767 V), and S_0RGO (0.733 V). This early onset potential is superior to or comparable with most of the carbon-based catalysts reported hitherto.[15,44–46] Regarding the kinetic current of H_2O_2 (j_k), it is notable that $S_{10}RGO$ exhibits the highest value of 34.7 mA cm^{-2} at 0.50 V, vastly exceeding those of S_1RGO (10.6 mA cm^{-2}), $S_{20}RGO$ (32.9 mA cm^{-2}) and S_0RGO (6.6 mA cm^{-2}) (Fig. 2d). However, the most active sample at a higher potential of 0.65 V is found to be $S_{20}RGO$ with a j_k value of 1.62 mA cm^{-2}. Fig. 2e shows the S_xRGO ($x = 1, 10, 20$) exhibit a smaller Tafel slope compared to that of S_0RGO, indicating the doped sulfur content favoring ORR kinetics. Importantly, the mass activity of sulfur-doped catalysts, as depicted in Fig. S17,† surpasses that of S_0RGO, with the highest value of 8.8 A g^{-1} observed for $S_{10}RGO$ at 0.75 V. This outperforms the performance of most reported carbon catalysts (Table S7†). The above results prove that incorporation of C–S and C–SO$_x$ groups could greatly enhance the selectivity and activity of S_xRGO ($x = 1, 10, 20$) towards $2e^-$ ORR, and the H_2O_2 selectivity and activity
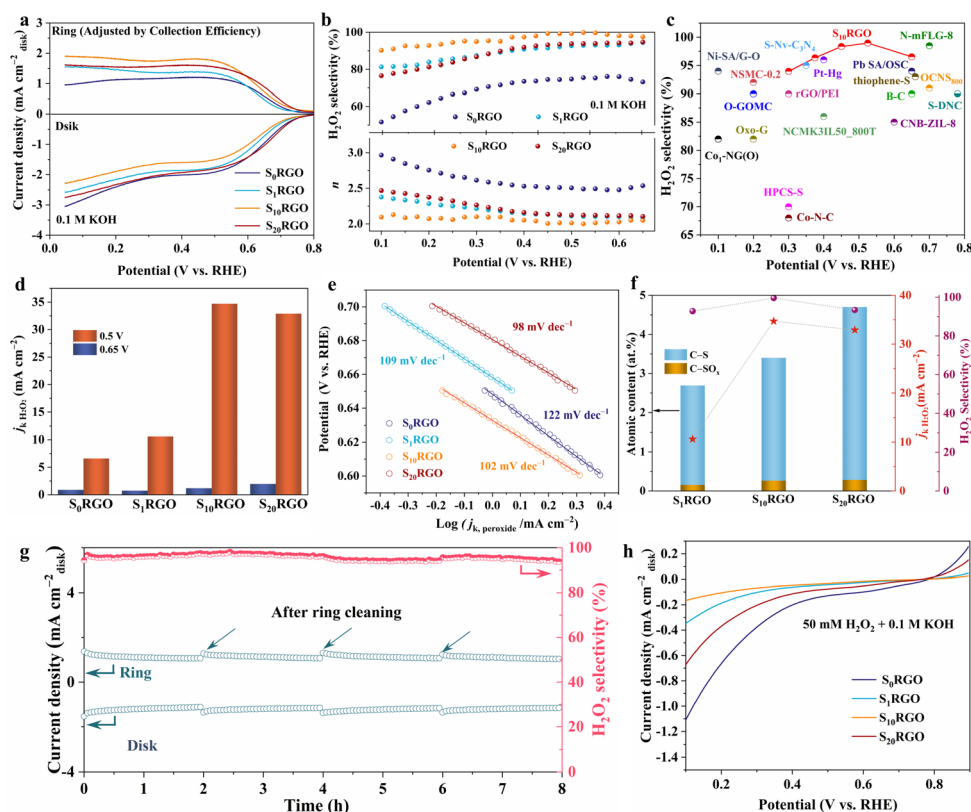

Fig. 2 (a) LSV curves, (b) H_2O_2 selectivity and electron transfer number of S_xRGO. (c) H_2O_2 selectivity on $S_{10}RGO$ and previously reported catalysts (as summarized in Table S6†) in alkaline solution. (d) Comparison of j_k at 0.5 V and 0.6 V. (e) Tafel plots. (f) Dependence of H_2O_2 selectivity and j_k on S moiety content. (g) Stability of $S_{10}RGO$ in 0.1 M KOH. (h) LSV curves of S_xRGO in 0.1 M KOH containing 50 mM H_2O_2. Catalyst loading: 143 μg cm^{-2}.

are dependent on the content of sulfur configurations (Fig. 2f and S18†). To further validate the catalytic trends induced by sulfur doping, two additional samples designated as S_5RGO and $S_{15}RGO$ were prepared. Their surface elemental compositions, chemical states, and electrocatalytic ORR performances were compared with those of S_xRGO (where $x = 1, 10, 20$) (Fig. S19†). The results confirmed the previously proposed structure–property correlation. The stability of $S_{10}RGO$ was assessed at a constant disk potential of 0.52 V (Fig. 2g), which shows that the H_2O_2 selectivity remained above 95% throughout 8 h of continuous electrolysis, showing commendable stability in an alkaline solution.

In addition, these sulfur-doped RGO samples exhibit remarkable selectivity towards H_2O_2 in a neutral solution (0.1 M Na_2SO_4) (Fig. S20†). As shown in Fig. S21,† the $S_{10}RGO$ displays significantly higher ring current and smaller disk current density with respect to the S_0RGO, showing excellent H_2O_2 generation performance with a selectivity of 89% and an electron transfer number of 2.2 at 0.4 V. It has been demonstrated that the H_2O_2 reduction reaction (PRR) on the catalyst is an important factor affecting the cumulative formation of H_2O_2, so the electrocatalytic PRR experiments were conducted in Ar-saturated 0.1 M KOH and 0.1 M Na_2SO_4 solutions containing 50 mM H_2O_2, respectively. As shown in Fig. 2h and S21c,† the $S_{10}RGO$ delivers the lowest reduction current density in both KOH (0.18 mA cm^{-2}) at 0.10 V and Na_2SO_4 (0.16 mA cm^{-2}) at 0 V, which should be another important parameter for its superior performance in H_2O_2 production.

Electrosynthesis of H_2O_2

By casting $S_{10}RGO$ onto a hydrophobic carbon paper with a loading of 600 μg cm^{-2}, the electrolysis experiment was conducted at 0.52 V using a custom-designed electrochemical H-type cell in O_2-saturated 0.1 M KOH solution under 400 rpm stirring (Fig. 3a and S22†). The H_2O_2 production rates and Faraday efficiency (FE) over S_xRGO were quantified by cerium sulfate (Ce(SO$_4$)$_2$) titration (Fig. S23†). As shown in Fig. 3b, the $S_{10}RGO$ displays a maximal H_2O_2 production rate (1853.85 ± 300 mmol g$_{cat}^{-1}$ h^{-1}) and maximum FE (96.51 ± 3%) after 1 h with respect to the other three samples. Specifically, the $S_{10}RGO$ exhibits an almost linear increase in H_2O_2 yield over 60 min (Fig. S24†). As shown in Fig. S25,† a steady current density of ∼5 mA cm^{-2} could be maintained after 90 h without an obvious decline. It should be pointed out that as depicted in Fig. S26,† the catalytic effect of the carbon paper electrode can be disregarded since both the current and H_2O_2 generation predominantly originated from the $S_{10}RGO$ catalyst. Furthermore, a gas diffusion electrode and a three-phase flow cell reactor (Fig. 3c) were employed to enhance the H_2O_2 productivity of $S_{10}RGO$ by circumventing the issue of low O_2 solubility in the aqueous electrolyte. The LSV curves were recorded in the flow-cell setup in 1.0 M KOH with manual 100% iR compensation. As depicted in Fig. 3d, the $S_{10}RGO$ demonstrates a significantly enhanced current density in an O_2 atmosphere with respect to an Ar atmosphere in the flow-cell. The substantial disparity between the O_2 and Ar atmospheres indicates the oxygen reduction
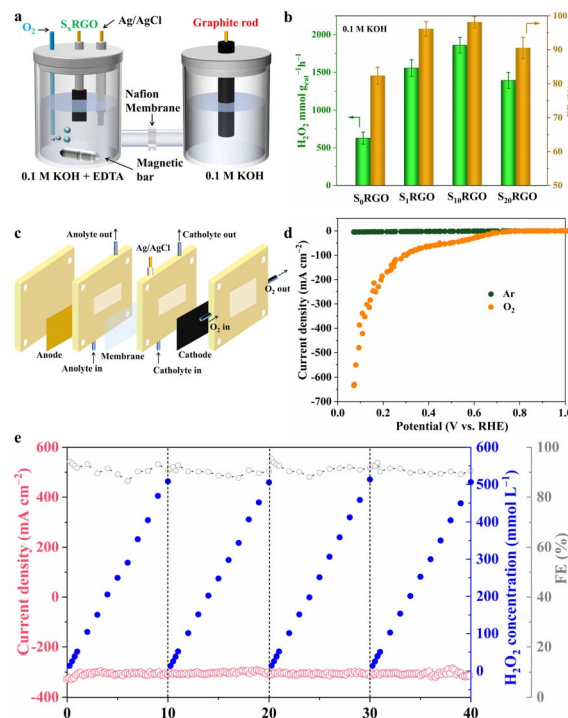

Fig. 3 (a) Schematic illustration of the H-type cell for H_2O_2 production. (b) H_2O_2 production rate and FE of S_xRGO in the H-type cell. (c) Schematic illustration of the flow cell setup for H_2O_2 production. (d) LSV curves of $S_{10}RGO$ tested under O_2 and Ar atmospheres in the flow-cell setup, respectively. (e) Chronoamperometry test of $S_{10}RGO$ at 0.15 V for H_2O_2 production in the flow cell using 1.0 M KOH as the electrolyte and FE. The electrolyte was refreshed every 10 h during the test. Catalyst loading: 600 μg cm^{-2}.

ability of the cathode. Moreover, it is found that the polarisation curve of $S_{10}RGO$ seems to experience a kind of plateau at 0.5–0.3 V vs. RHE before a second wave kicks in, which is different from S_0RGO (Fig. S27†). This unusual shape of the polarization curve shares similarities with the enhanced ring current density observed in LSV curves below 0.3 V (Fig. 2a). This phenomenon may stem from the oxidation of some of the C–S bonds to C–SO$_x$ species during accumulation of H_2O_2 from 0.5 to 0.3 V, which would influence the interfacial interaction between the catalyst and H_2O (Fig. S28†).[34] This hypothesis was further proved by EIS measurements (Fig. S29 and S30†), which indicated that the mass transport kinetics was retarded in $S_{10}RGO$ in the potential range of 0.3–0 V, thereby creating favorable interfacial conditions for selective H_2O_2 synthesis through inhibiting the attack of H_2O_2 by active hydrogen.[47] Surprisingly, the $S_{10}RGO$ attains a remarkable current density of up to 500 mA cm^{-2} at a low potential of merely 0.10 V, manifesting significant potential for industrial applications. During the bulk electrolysis at different potentials, a high current density ranging from 50 to 300 mA cm^{-2} can be consistently maintained without noticeable degradation for at least 40 h, respectively (Fig. S31–S33†). Moreover, at an industrial current density of 300 mA cm^{-2}, the $S_{10}RGO$ exhibited an average FE% of approximately 90.5% and achieved a high production rate of 9.33 ± 0.19 mol g^{-1} h^{-1},

respectively. Compared to literature catalysts (Table 1), S_{10}RGO's wide operational window and balanced performance metrics underscore its potential for industrial-scale applications. The concentration of the accumulated H_2O_2 increased almost linearly and reached 508.2 mmol L^{-1} after about 10 h of electrolysis, which could be stably operated for 4 cycles and produced 0.4 L of 508.2 mmol per L H_2O_2 solution (Fig. 3e). The long-term accumulation of H_2O_2 at a potential of 0.15 V over a period of 29 h was executed in a flow cell containing 100 mL of alkaline electrolyte, as illustrated in Fig. S34;† throughout this interval, the cumulative amount of H_2O_2 reached a significant 857.5 mmol L^{-1} (equivalent to 3.0 wt%), which is deemed adequate for the production of medical-grade disinfectants.[55] These results emphasize the capability of S_{10}RGO for continuous and stable production of H_2O_2, suggesting its significant potential as a feasible candidate for large-scale H_2O_2 electrosynthesis in industrial applications.

Understanding the underlying mechanism

To detect the key adsorbed oxygen intermediate on the S_{10}RGO during electrocatalytic H_2O_2 synthesis, *in situ* attenuated total reflectance surface-enhanced infrared absorption spectra (ATR-SEIRAS) were recorded at different time intervals and potentials in the O_2-saturated 0.10 M Na_2SO_4 and 0.10 M KOH solution (Fig. 4a and S35†). Notably, two new absorption peaks at ~1240 cm^{-1} and 1420 cm^{-1} emerged and increased over time, which can be assigned to the O–O stretching vibration of OOH* and O–O stretching mode of adsorbed molecular oxygen ($O_{2,ad}$), respectively.[56,57] Therefore, the ATR-SEIRAS results supported the OOH*-mediated 2e⁻ ORR pathway.

Secondly, the sulfur-containing molecule investigations were designed and conducted to uncover the effects of C–S and sulfur oxide species in the 2e⁻ ORR.[58] Small organic molecules including dibenzothiophene (DS), sulfobenzide (SO) and their mixture were selected as heterogeneous catalysts. Their electrocatalytic ORR performances were evaluated *via* a similar process. Meanwhile, comparison experiments using a blank RRDE or a 5% Nafion solution modified RRDE were performed. It is important to highlight that, owing to the distinct differences in interaction modes, interface environments, and accessibility of active sites between sulfur-containing molecule-loaded heterogeneous catalysts and sulfur-doped carbon solid catalysts, the electrocatalytic performance of molecular catalysts is significantly inferior to that of sulfur-doped carbon catalysts in terms of both activity and selectivity. Interestingly, as shown in Fig. 4b and c, the mixture of DS and SO exhibited superior performance in terms of H_2O_2 selectivity, kinetic current of H_2O_2 and Tafel slope as compared to other single catalysts (Fig. S36†). This phenomenon further supports the above research results that the C–S and C–SO_2 groups show a synergistic effect in driving 2e⁻ ORR.

Finally, to reveal the role of different sulfur configurations in electrocatalytic 2e⁻ ORR, DFT calculations were employed to simulate the charge density, H_2O_2 formation pathway and Fermi levels of three typical catalysts (S-RGO, SO_x-RGO, and S/SO_x-RGO) containing different sulfur configurations (Fig. S37†). The 2e⁻ ORR pathway exclusively involves the intermediate OOH*, while further reducing OOH* generates intermediates (O* and OH*) that proceed *via* the 4e⁻ ORR pathway. It has been reported that the formation of the OOH* intermediate is the rate-limiting step for achieving selectivity towards H_2O_2.[59] As seen in Fig. 4e and S38,† the first step (O_2* → OOH*) over the RGO and SO_x-RGO is shown to be endergonic, while the S-RGO and S/SO_x-RGO exhibit exergonic behavior. In other words, the challenging limiting step on the RGO and SO_x-RGO surfaces becomes facile on the S-RGO and S/SO_x-RGO surfaces. Compared to S-RGO, S/SO_x-RGO further reduces the energy barrier of the limiting step O_2* → OOH*. Besides, the free energy drop for H_2O_2 formation (OOH* → H_2O_2) over S/SO_x-RGO (−0.84 eV) is slightly larger than that over S-RGO (−0.83 eV), indicating a favorable propensity for H_2O_2 production over S/SO_x-RGO. Additionally, the formation energy of OOH* to O* is

Table 1 Performance parameters of S_{10}RGO and various reported catalysts in alkaline media

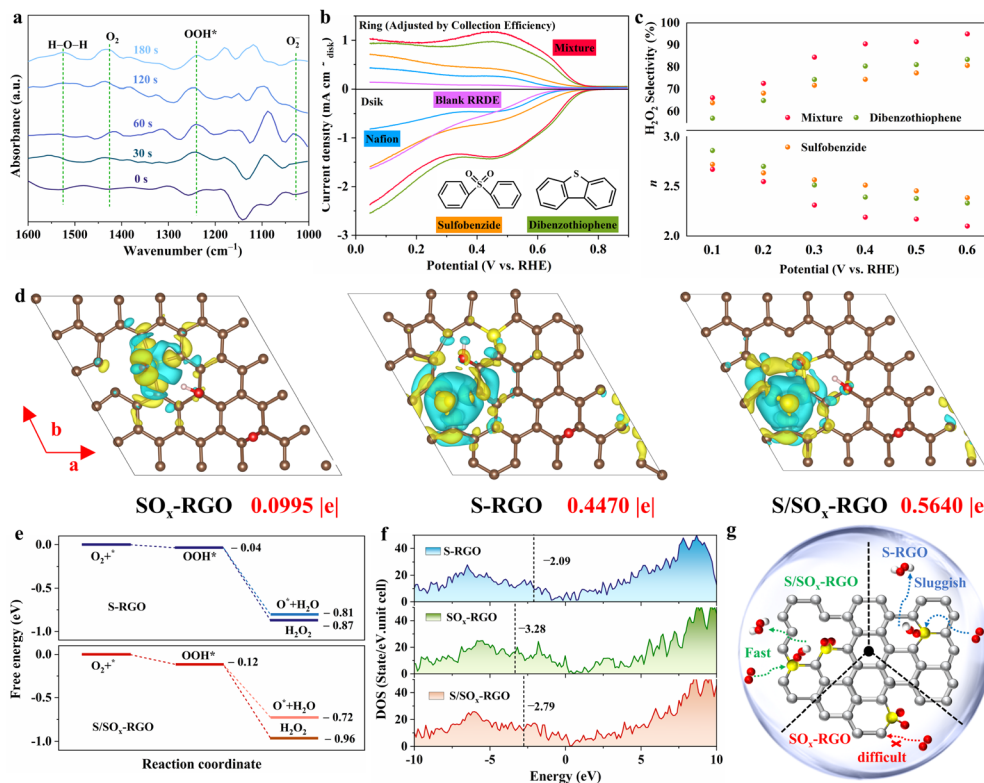| Catalyst	Selectivity (%)	Stability	Production (mol g_{cat}^{-1} h^{-1})	FE (%)
S_{10}RGO	90–98.9% @ 0.1–0.65 V	40 h @ 300 mA cm^{-2}	9.33 ± 0.19	~90.5
		50 h @ 120 mA cm^{-2}	6.74 ± 0.18	~91
This work		50 h @ 50 mA cm^{-2}	4.28 ± 0.15	~91.3
N-mFLG-8 (ref. 16)	95–98.5% @ 0.3–0.7 V	50 h @ 20 mA cm^{-2}	9.66	~100
OCNS$_{900}$ (ref. 48)	90–91% @ 0.55–0.75 V	11 h @ 50 mA cm^{-2}	0.77	—
CNB-ZIL-8 (ref. 49)	80–85% @ 0.2–0.6 V	9 h @ 40 mA cm^{-2}	1.787	~80
Thiophene-S[29]	90–93% @ 0.5–0.75 V	8 h @ 20 mA cm^{-2}	3.46	~92.8
HPCS-S[25]	70% @ 0.3 V	—	183.99 (H-cell)	—
S-DNC[26]	90% @ 0.78 V	—	4.05 (H-cell)	~100
S-Nv-C_3N_4 (ref. 27)	95% @ 0.35 V	24 h @ 200 mA cm^{-2}	4.52 (H-cell)	~80
S-mC-0.375 (ref. 30)	92–99% @ 0.2–0.7 V	24 h @ 185 mA cm^{-2}	25	~95
B–C[15]	90.5% @ 0.65 V	30 h @ 200 mA cm^{-2}	—	85–90
Co_1–NG(O)[8]	82% @ 0.1 V	110 h @ 5 mA cm^{-2}	—	~93
Pb–SA/OSC[50]	90–94% @ 0.3–0.7 V	2 h @ 400 mA cm^{-2}	0.69	~92.7
Co HSACs[51]	95% @ 0.5–0.75 V	25 h @ 300 mA cm^{-2}	—	~90
NBO–G/CNTs[52]	80–100% @ 0.2–0.7 V	12 h @ 50 mA cm^{-2}	0.709	~80
Co–N_5–O–C SACs[53]	80–85% @ 0.3–0.75 V	24 h @ 100 mA cm^{-2}	5.92	~80
Sb-NSCF[54]	90–97.2% @ 0.4–0.7 V	75 h @ 50 mA cm^{-2}	7.46	~80

Fig. 4 (a) ATR-SEIRAS spectra recorded on $S_{10}RGO$ at different time intervals in O_2-saturated 0.10 M Na_2SO_4. (b) LSV curves and (c) H_2O_2 selectivity of standalone molecules and their mixture. Catalyst loading: 143 μg cm^{-2}. (d) Differential charge densities of SO_x-RGO, S-RGO and S/SO_x-RGO. Yellow and cyan isosurfaces show the electron gain and electron loss, respectively. (e) The free energy variations for the S-RGO and S/SO_x-RGO during 2e$^-$ and 4e$^-$ ORR. (f) The density of states (DOS) for SO_x-RGO, S-RGO and S/SO_x-RGO. The dashed lines are Fermi levels. (g) Schematic diagram of two-electron pathways on S_xRGO with different S configurations.

higher over S/SO_x-RGO (−0.60 eV) compared to that over S-RGO (−0.77 eV), indicating its reduced susceptibility to the 4e$^-$ process. Therefore, the ORR activity trend follows the order: RGO < SO_x-RGO < S-RGO < S/SO_x-RGO, and the S/SO_x-RGO serves as a highly favorable catalyst for 2e$^-$ ORR, which agrees with the S_xRGO experimental and standalone molecule investigation results.

The effects of the functional groups on the formation of OOH* and H_2O_2 can be further explained by the charge density and Fermi levels. As depicted in Fig. 4d, the charge depletion is shown as the region of C atoms near sulfur oxide on the SO_x-RGO (0.0995 e$^-$), whereas in the cases of S-RGO and S/SO_x-RGO, the charge state of the S atom becomes more positive by 0.5640 e$^-$ and 0.4470 e$^-$, respectively, in qualitative agreement with that of the previous report.[60] This suggests that the C–S group is primarily utilized to increase the charge state of the S atom, while the electronic charge is depleted towards the neighboring C atoms, specifically facilitating the originally difficult rate-limiting step (O_2* → OOH*) over RGO. Meanwhile, when both C–S and C–SO_x groups coexist in the RGO, the electron-poor sulfur center serves as O_2 adsorption sites on the graphitic carbon matrix, which facilitates the adsorption of O_2 molecules and reduces the barrier to O_2* → OOH*. On the other hand, as shown in Fig. 4f, the presence of the C–SO_x group can lower the Fermi level of the catalyst compared to the C–S

group. This decrease in Fermi level weakens the adsorption of the OOH* intermediate since it becomes more challenging to donate electrons from the catalyst, which facilitates the release of OOH* and effectively prevents the 2e$^-$ + 2e$^-$ reaction mechanism.[8] As a consequence, the C–S and C–SO_x groups play distinct yet complementary roles in the electrocatalytic 2e$^-$ ORR. The suitable sulfur configuration and proportion gives rise to favorable formation and optimal adsorption strength of the *OOH intermediate, further achieving exceptional 2e$^-$ ORR selectivity for the sulfur-doped carbon material (Fig. 4g).

4 Conclusions

In this work, the C–S and C–SO_x active centers in sulfur-doped RGO materials (S_xRGO) for 2e$^-$ ORR were successfully constructed and identified on the basis of an experimental investigation and theoretical calculations. By temperature-programmed annealing and adjusting the mass ratio of precursor materials, the sulfur configurations on the S_xRGO catalysts can be tuned and optimized. The C–S and C–SO_x groups have complementary effects during 2e$^-$ ORR, in which the C–S group greatly drives the rate-limiting step (O_2* → OOH*) by increasing the charge state of the S atom and promoting adsorption of O_2, while C–SO_x species modulate the ORR pathway through both electronic and interfacial effects,

weakening OOH* adsorption and tuning proton transfer dynamics. Finally, the optimized sulfur configurations on the $S_{10}RGO$ catalyst exhibit excellent $2e^-$ ORR performance in alkaline media, with a maximum selectivity of 98.9% for electrochemical H_2O_2 synthesis and selectivity exceeding 90% across a wide voltage range of 0.1–0.65 V. The $S_{10}RGO$ exhibits a current density of up to 500 mA cm^{-2} for H_2O_2 production in a flow cell device, achieving a production rate of 9.33 ± 0.19 mol $g_{cat}^{-1} h^{-1}$ and maintaining a stable FE of 90.5% during the ORR at a current density of 300 mA cm^{-2} for 40 h. Our findings should contribute to developing efficient carbon-based catalysts for electrocatalytic production of H_2O_2 in practical industrial applications.

Data availability

The data that support the findings of this study are available from the corresponding authors upon reasonable request.

Author contributions

Sifan Li: investigation, data curation, formal analysis, visualization, writing – original draft. Shiwen Du: investigation, data curation, software, writing – original draft, writing – review & editing. Jiansheng Li: conceptualization, methodology, validation, writing – review & editing, supervision, funding acquisition. Wenjun Fan: formal analysis, methodology. Yang Yang: formal analysis, methodology. Peng Zhao: data curation, visualization. Haotian Zhu: software, validation. Wansheng You: methodology, visualization. Xiaojing Sang: formal analysis, methodology, validation, writing – review & editing. Fuxiang Zhang: conceptualization, methodology, validation, writing – review & editing.

Conflicts of interest

There are no conflicts to declare.

Acknowledgements

References

1 Y. Y. Yan, W. J. Niu, W. W. Zhao, R. J. Li, E. P. Feng, B. X. Yu, B. K. Chu and C. Y. Cai, Recent advances and future perspectives of transition metal-supported carbon with different dimensions for highly efficient electrochemical hydrogen peroxide preparation, *Adv. Energy Mater.*, 2024, **14**, 2303506.

2 Z. Deng, S. J. Choi, G. Li and X. Wang, Advancing H_2O_2 electrosynthesis: enhancing electrochemical systems, unveiling emerging applications, and seizing opportunities, *Chem. Soc. Rev.*, 2024, **53**, 8137–8181.

3 E. A. Moges, C.-Y. Chang, W.-H. Huang, F. T. Angerasa, K. Lakshmanan, T. M. Hagos, H. G. Edao, W. B. Dilebo, C.-W. Pao and M.-C. Tsai, Heteroatom-coordinated palladium molecular catalysts for sustainable electrochemical production of hydrogen peroxide, *J. Am. Chem. Soc.*, 2023, **146**, 419–429.

4 S. Yang, A. Verdaguer-Casadevall, L. Arnarson, L. Silvioli, V. Čolić, R. Frydendal, J. Rossmeisl, I. Chorkendorff and I. E. L. Stephens, Toward the decentralized electrochemical production of H_2O_2: a focus on the catalysis, *ACS Catal.*, 2018, **8**, 4064–4081.

5 N. Dhanda, Y. K. Panday and S. Kumar, Recent advances in the electrochemical production of hydrogen peroxide, *Electrochim. Acta*, 2024, **481**, 143872.

6 N. Wang, S. Ma, P. Zuo, J. Duan and B. Hou, Recent progress of electrochemical production of hydrogen peroxide by two-electron oxygen reduction reaction, *Adv. Sci.*, 2021, **8**, 2100076.

7 X. Ren, X. Dong, L. Liu, J. Hao, H. Zhu, A. Liu and G. Wu, Research progress of electrocatalysts for the preparation of H_2O_2 by electrocatalytic oxygen reduction reaction, *SusMat*, 2023, **3**, 442–470.

8 E. Jung, H. Shin, B. H. Lee, V. Efremov, S. Lee, H. S. Lee, J. Kim, W. Hooch Antink, S. Park, K. S. Lee, S. P. Cho, J. S. Yoo, Y.-E. Sung and T. Hyeon, Atomic-level tuning of Co–N–C catalyst for high-performance electrochemical H_2O_2 production, *Nat. Mater.*, 2020, **19**, 436–442.

9 J. S. Lim, J. Woo, G. Bae, S. Yoo, J. Kim, J. H. Kim, J. H. Lee, Y. J. Sa, J.-W. Jang, Y. J. Hwang, C. H. Choi and S. H. Joo, Understanding the preparative chemistry of atomically dispersed nickel catalysts for achieving high-efficiency H2O2 electrosynthesis, *Chem. Sci.*, 2024, **15**, 13807–13822.

10 R. Wang, J. Zhong, D. Li, J. Meng, W. Huang, X. Ma, W. Guo, F. Tian and C. Li, Engineering *d*-band center of cobalt active sites via dual coordination with nitrogen-doped carbon nanotube and $Ti_3C_2T_x$ mXene toward electrocatalytic oxygen reduction for H_2O_2 production, *Chem. Eng. J.*, 2024, **488**, 150894.

11 M. Song, W. Liu, J. Zhang, C. Zhang, X. Huang and D. Wang, Single-atom catalysts for H_2O_2 electrosynthesis via two-electron oxygen reduction reaction, *Adv. Funct. Mater.*, 2023, **33**, 2212087.

12 B. Reuillard, S. Gentil, M. Carrière, A. Le Goff and S. Cosnier, Biomimetic versus enzymatic high-potential electrocatalytic reduction of hydrogen peroxide on a functionalized carbon nanotube electrode, *Chem. Sci.*, 2015, **6**, 5139–5143.

13 C. Ouyang, B. Ni, Z. Sun, J. Zhuang, H. Xiao and X. Wang, Boosting the ORR performance of modified carbon black via C–O bonds, *Chem. Sci.*, 2019, **10**, 2118–2123.

14 J. Du, Q. Han, Y. Chen, M. Peng, L. Xie and A. Chen, Micro/meso-porous double-shell hollow carbon spheres through spatially confined pyrolysis for supercapacitors and zinc-Ion capacitor, *Angew. Chem., Int. Ed.*, 2024, **63**, e202411066.

15 Y. Xia, X. Zhao, C. Xia, Z.-Y. Wu, P. Zhu, J. Y. Kim, X. Bai, G. Gao, Y. Hu, J. Zhong, Y. Liu and H. Wang, Highly active

and selective oxygen reduction to H_2O_2 on boron-doped carbon for high production rates, *Nat. Commun.*, 2021, **12**, 4225.

16 L. Li, C. Tang, Y. Zheng, B. Xia, X. Zhou, H. Xu and S. Z. Qiao, Tailoring selectivity of electrochemical hydrogen peroxide generation by tunable pyrrolic-nitrogen-carbon, *Adv. Energy Mater.*, 2020, **10**, 2000789.

17 J. S. Lim, J. H. Kim, J. Woo, D. S. Baek, K. Ihm, T. J. Shin, Y. J. Sa and S. H. Joo, Designing highly active nanoporous carbon H_2O_2 production electrocatalysts through active site identification, *Chem*, 2021, **7**, 3114–3130.

18 J. Du, X. Peng, X. Gao, J. Li, Q. Han, J. Guan and A. Chen, Engineering three-dimensional interconnected pores with plentiful edge sites via a confined space for enhanced oxygen reduction, *Nano Lett.*, 2024, **24**, 12140–12147.

19 Z. Ma, S. Dou, A. Shen, L. Tao, L. Dai and S. Wang, Sulfur-doped graphene derived from cycled lithium–sulfur batteries as a metal-free electrocatalyst for the oxygen reduction reaction, *Angew. Chem., Int. Ed.*, 2015, **54**, 1888–1892.

20 X. Feng, Y. Bai, M. Liu, Y. Li, H. Yang, X. Wang and C. Wu, Untangling the respective effects of heteroatom-doped carbon materials in batteries, supercapacitors and the ORR to design high performance materials, *Energy Environ. Sci.*, 2021, **14**, 2036–2089.

21 I. Y. Jeon, S. Zhang, L. Zhang, H. J. Choi, J. M. Seo, Z. Xia, L. Dai and J. B. Baek, Edge-selectively sulfurized graphene nanoplatelets as efficient metal-free electrocatalysts for oxygen reduction reaction: the electron spin effect, *Adv. Mater.*, 2013, **25**, 6138–6145.

22 F. Xiang, X. Zhao, J. Yang, N. Li, W. Gong, Y. Liu, A. Burguete-Lopez, Y. Li, X. Niu and A. Fratalocchi, Enhanced selectivity in the electroproduction of H_2O_2 via F/S dual-doping in metal-free nanofibers, *Adv. Mater.*, 2023, **35**, 2208533.

23 J. Xu, Y. Cui, M. Wang, G. Chai and L. Guan, Pyrimidine-assisted synthesis of S, N-codoped few-layered graphene for highly efficient hydrogen peroxide production in acid, *Chem Catal.*, 2022, **2**, 1450–1466.

24 B. Dou, G. Wang, X. Dong and X. Zhang, Improved H_2O_2 electrosynthesis on S-doped Co–N–C through cooperation of Co–S and thiophene S, *ACS Appl. Mater. Interfaces*, 2024, **16**, 7374–7383.

25 G. Chen, J. Liu, Q. Li, P. Guan, X. Yu, L. Xing, J. Zhang and R. Che, A direct H_2O_2 production based on hollow porous carbon sphere-sulfur nanocrystal composites by confinement effect as oxygen reduction electrocatalysts, *Nano Res.*, 2019, **12**, 2614–2622.

26 W. Shen, C. Zhang, X. Wang, Y. Huang, Z. Du, M. Alomar, J. Wang, J. Lv, J. Zhang and X. Lu, Sulfur-doped defective nanocarbons derived from fullerenes as electrocatalysts for efficient and selective H_2O_2 electroproduction, *ACS Mater. Lett.*, 2024, **6**, 17–26.

27 S. Xu, Y. Yu, X. Zhang, D. Xue, Y. Wei, H. Xia, F. Zhang and J. Zhang, Enhanced electron delocalization induced by ferromagnetic sulfur doped C_3N_4 triggers selective H_2O_2 production, *Angew. Chem., Int. Ed.*, 2024, **136**, e202407578.

28 H. Kim, H. Yang, J. Kang and N. Takeuchi, Multifunctional disordered sulfur-doped carbon for efficient sodium-ion-exchange and 2-electron-transfer-dominant oxygen reduction reaction, *Carbon*, 2021, **182**, 242–253.

29 R. Xie, C. Cheng, R. Wang, J. Li, E. Zhao, Y. Zhao, Y. Liu, J. Guo, P. Yin and T. Ling, Maximizing thiophene–sulfur functional groups in carbon catalysts for highly selective H_2O_2 electrosynthesis, *ACS Catal.*, 2024, **14**, 4471–4477.

30 J. Du, Y. Liu, M. Sun, J. Guan, A. Chen and B. Han, Highly selective oxygen electroreduction to hydrogen peroxide on sulfur-doped mesoporous carbon, *Angew. Chem., Int. Ed.*, 2025, e202503385.

31 Y. Fang, Y. Fan, K. Xie, W. Ge, Y. Zhu, Z. Qi, Z. Song, H. Jiang and C. Li, Boosting hydrogen peroxide electrosynthesis via modulating the interfacial hydrogen-bond environment, *Angew. Chem., Int. Ed.*, 2023, **62**, e202304413.

32 H. Sheng, E. D. Hermes, X. Yang, D. Ying, A. N. Janes, W. Li, J. R. Schmidt and S. Jin, Electrocatalytic production of H_2O_2 by selective oxygen reduction using earth-abundant cobalt pyrite (CoS_2), *ACS Catal.*, 2019, **9**, 8433–8442.

33 G. Kresse and J. Furthmüller, Efficient iterative schemes for ab initio total-energy calculations using a plane-wave basis set, *Phys. Rev. B: Condens. Matter Mater. Phys.*, 1996, **54**, 11169–11186.

34 P. E. Blöchl, Projector augmented-wave method, *Phys. Rev. B: Condens. Matter Mater. Phys.*, 1994, **50**, 17953–17979.

35 J. P. Perdew, J. A. Chevary, S. H. Vosko, K. A. Jackson, M. R. Pederson, D. J. Singh and C. Fiolhais, Atoms, molecules, solids, and surfaces: applications of the generalized gradient approximation for exchange and correlation, *Phys. Rev. B: Condens. Matter Mater. Phys.*, 1992, **46**, 6671–6687.

36 J. P. Perdew, K. Burke and M. Ernzerhof, Generalized gradient approximation made simple, *Phys. Rev. Lett.*, 1996, **77**, 3865–3868.

37 H. J. Monkhorst and J. D. Pack, Special points for Brillouin-zone integrations, *Phys. Rev. B*, 1976, **13**, 5188–5192.

38 A. Bagri, C. Mattevi, M. Acik, Y. J. Chabal, M. Chhowalla and V. B. Shenoy, Structural evolution during the reduction of chemically derived graphene oxide, *Nat. Chem.*, 2010, **2**, 581–587.

39 Y. S. Yun, V. D. Le, H. Kim, S. J. Chang, S. J. Baek, S. Park, B. H. Kim, Y. H. Kim, K. Kang and H. J. Jin, Effects of sulfur doping on graphene-based nanosheets for use as anode materials in lithium-ion batteries, *J. Power Sources*, 2014, **262**, 79–85.

40 M. G. Ersozoglu, H. Gursu, M. Gencten, A. S. Sarac and Y. Sahin, A green approach to fabricate binder-free S-doped graphene oxide electrodes for vanadium redox battery, *Int. J. Energy Res.*, 2020, **45**, 2126–2137.

41 Y. Guo, Z. Zeng, Y. Zhu, Z. Huang, Y. Cui and J. Yang, Catalytic oxidation of aqueous organic contaminants by persulfate activated with sulfur-doped hierarchically porous carbon derived from thiophene, *Appl. Catal., B*, 2018, **220**, 635–644.

42 Y. Su, Y. Zhang, X. Zhuang, S. Li, D. Wu, F. Zhang and X. Feng, Low-temperature synthesis of nitrogen/sulfur co-

doped three-dimensional graphene frameworks as efficient metal-free electrocatalyst for oxygen reduction reaction, *Carbon*, 2013, **62**, 296–301.

43 M. Li, C. Liu, H. Zhao, H. An, H. Cao, Y. Zhang and Z. Fan, Tuning sulfur doping in graphene for highly sensitive dopamine biosensors, *Carbon*, 2015, **86**, 197–206.

44 Z. Lu, G. Chen, S. Siahrostami, Z. Chen, K. Liu, J. Xie, L. Liao, T. Wu, D. Lin and Y. Liu, High-efficiency oxygen reduction to hydrogen peroxide catalysed by oxidized carbon materials, *Nat. Catal.*, 2018, **1**, 156–162.

45 H. Xu, S. Zhang, X. Zhang, M. Xu, J. Geng, M. Han and H. Zhang, Melamine sponge templated synthesis of nickel nanoparticles encapsulated in B, N co-doped carbon nanotubes towards the selective electrosynthesis of hydrogen peroxide, *J. Mater. Chem. A*, 2023, **11**, 10204–10212.

46 D. Iglesias, A. Giuliani, M. Melchionna, S. Marchesan, A. Criado, L. Nasi, M. Bevilacqua, C. Tavagnacco, F. Vizza, M. Prato and P. Fornasiero, N-doped graphitized carbon nanohorns as a forefront electrocatalyst in highly selective O_2 Reduction to H_2O_2, *Chem*, 2018, **4**, 106–123.

47 Y. Fan, Y. Chen, W. Ge, L. Dong, Y. Qi, C. Lian, X. Zhou, H. Liu, Z. Liu, H. Jiang and C. Li, Mechanistic insights into surfactant-modulated electrode-electrolyte interface for steering H_2O_2 electrosynthesis, *J. Am. Chem. Soc.*, 2024, **146**, 7575–7583.

48 S. Chen, T. Luo, K. Chen, Y. Lin, J. Fu, K. Liu, C. Cai, Q. Wang, H. Li and X. Li, Chemical identification of catalytically active sites on oxygen-doped carbon nanosheet to decipher the high activity for electro-synthesis hydrogen peroxide, *Angew. Chem., Int. Ed.*, 2021, **133**, 16743–16750.

49 Z. Tian, Q. Zhang, L. Thomsen, N. Gao, J. Pan, R. Daiyan, J. Yun, J. Brandt, N. López-Salas, F. Lai, Q. Li, T. Liu, R. Amal, X. Lu and M. Antonietti, Constructing interfacial boron-nitrogen moieties in turbostratic carbon for electrochemical hydrogen peroxide production, *Angew. Chem., Int. Ed.*, 2022, **61**, e202206915.

50 X. Zhou, Y. Min, C. Zhao, C. Chen, M.-K. Ke, S.-L. Xu, J.-J. Chen, Y. Wu and H.-Q. Yu, Constructing sulfur and oxygen super-coordinated main-group electrocatalysts for selective and cumulative H_2O_2 production, *Nat. Commun.*, 2024, **15**, 193.

51 W. Fan, Z. Duan, W. Liu, R. Mehmood, J. Qu, Y. Cao, X. Guo, J. Zhong and F. Zhang, Rational design of heterogenized molecular phthalocyanine hybrid single-atom electrocatalyst towards two-electron oxygen reduction, *Nat. Commun.*, 2023, **14**, 1426.

52 M. Fan, Z. Wang, K. Sun, A. Wang, Y. Zhao, Q. Yuan, R. Wang, J. Raj, J. Wu, J. Jiang and L. Wang, N–B–OH site-activated graphene quantum dots for boosting electrochemical hydrogen peroxide production, *Adv. Mater.*, 2023, **35**, 2209086.

53 W. Zhang, J. W. Choi, S. Kim, T. T. Le, S. Nandy, C.-K. Hwang, S. Y. Paek, A. Byeon, K. H. Chae, S. Y. Lee, S. H. Kim, H. Song, J. Kim, J. Oh, J. W. Lee, S. S. Han and J. M. Kim, Penta nitrogen coordinated cobalt single atom catalysts with oxygenated carbon black for electrochemical H_2O_2 production, *Appl. Catal., B*, 2023, **331**, 122712.

54 M. Yan, Z. Wei, Z. Gong, B. Johannessen, G. Ye, G. He, J. Liu, S. Zhao, C. Cui and H. Fei, Sb_2S_3-templated synthesis of sulfur-doped Sb-N-C with hierarchical architecture and high metal loading for H_2O_2 electrosynthesis, *Nat. Commun.*, 2023, **14**, 368.

55 Y. Zeng and G. Wu, Electrocatalytic H_2O_2 generation for disinfection, *Chin. J. Catal.*, 2021, **42**, 2149–2163.

56 C. Tang, L. Chen, H. Li, L. Li, Y. Jiao, Y. Zheng, H. Xu, K. Davey and S. Z. Qiao, Tailoring acidic oxygen reduction selectivity on single-atom catalysts via modification of first and second coordination spheres, *J. Am. Chem. Soc.*, 2021, **143**, 7819–7827.

57 S. Chen, T. Luo, X. Li, K. Chen, J. Fu, K. Liu, C. Cai, Q. Wang, H. Li and Y. Chen, Identification of the highly active Co–N_4 coordination motif for selective oxygen reduction to hydrogen peroxide, *J. Am. Chem. Soc.*, 2022, **144**, 14505–14516.

58 G. F. Han, F. Li, W. Zou, M. Karamad, J. P. Jeon, S. W. Kim, S. J. Kim, Y. Bu, Z. Fu, Y. Lu, S. Siahrostami and J. B. Baek, Building and identifying highly active oxygenated groups in carbon materials for oxygen reduction to H_2O_2, *Nat. Commun.*, 2020, **11**, 2209.

59 V. Viswanathan, H. A. Hansen, J. Rossmeisl and J. K. Nørskov, Unifying the $2e^-$ and $4e^-$ reduction of oxygen on metal surfaces, *J. Phys. Chem. Lett.*, 2012, **3**, 2948–2951.

60 D. Higgins, M. A. Hoque, M. H. Seo, R. Wang, F. Hassan, J. Y. Choi, M. Pritzker, A. Yu, J. Zhang and Z. Chen, Development and simulation of sulfur-doped graphene supported platinum with exemplary stability and activity towards oxygen reduction, *Adv. Funct. Mater.*, 2014, **24**, 4325–4336.